Vortex Shedding Behind a Rising Bubble and Two-Bubble Coalescence: a Numerical Approach

Anton Smolianski[a], Heikki Haario[b] and Pasi Luukka[b]

[a] *Institute of Mathematics, Zurich University, CH-8057 Zurich, Switzerland*
[b] *Laboratory of Applied Mathematics, Lappeenranta University of Technology, P.O. Box 20, FIN-53851 LPR, Finland*

Abstract

In this work, we present the computational results on the wake instability in wobbling bubble regime as well as on the coalescence of two bubbles in different shape regimes. This is a continuation of our previous studies on the dynamics of a single gas bubble rising in a viscous liquid (see (Smolianski et al. 2003)), and we use the same, finite-element/level-set/operator-splitting method that was proposed in (Smolianski 2001). The numerical method allows to simulate a wide range of flow regimes, accurately capturing the shape of the deforming interface of the bubble and the surface tension effect, while maintaining a good mass conservation. Due to the highly unstable and small-scale nature of the considered problems there are very few experimental investigations, but the comparison with available experimental data confirms a good accuracy of our numerical predictions. Our studies show that plausible results can be obtained with two-dimensional numerical simulations, when a single buoyant bubble or a coalescence of two bubbles is considered.

Key words: Two-phase flow, bubble dynamics, Navier-Stokes equations, finite elements, level set, operator splitting

1 Introduction

The rise of a gas bubble in a viscous liquid is a very complicated, non-linear and non-stationary hydrodynamical process. It is usually accompanied by a significant deformation of the bubble, indicating a complex interplay between fluid convection, viscosity and surface tension. The diverse shapes of the bubble resulting from this deformation cause a large variety of flow patterns around the bubble, and vice versa. A number of experimental studies have addressed this problem. Early studies include the rise of a bubble in an inviscid and a viscous

liquid, see (Hartunian & Sears 1957), (Walters & Davidson 1962) (Walters & Davidson 1963), (Wegener & Parlange 1973) and (Bhaga & Weber 1981). Approximate theoretical solutions have been obtained for either low (Taylor & Acrivos 1964) or high (Moore 1959) Reynolds numbers under the assumption that the bubble remains nearly spherical.

In the present paper, we attempt to model the full problem on the evolution of deformable gas bubble taking into account the surface tension force as well as the viscosity and density of the fluid inside of the bubble. We employ the level-set (see (Sethian 1999)) method that permits to compute topological changes of the interface (like mergers or breakups) and the finite element method that relies on a global variational formulation and, thus, naturally incorporates the coefficient jumps and the singular interface-concentrated force. The combination of finite elements with the level-set technique allows us to localize the interface precisely, without an introduction of any artificial parameters like the interface thickness. As a whole, our computational method takes an advantage of combining the finite element spatial discretization, the operator-splitting temporal discretization and the level-set interface representation.

Using the proposed computational method we provide a systematic study of diverse shape regimes for a single buoyant bubble, recovering all main regimes in a full agreement with available experimental data (for detailed analysis see (Smolianski et al. 2003)). In particular, we simulate a very unstable wobbling-bubble regime characterized by the non-symmetric vorticity pattern in the wake. The vortex shedding behind a rising wobbling bubble seems to be numerically simulated for the first time. Finally, we present the results on the bubble coalescence phenomena, emphasizing the main differences in the merger process for diverse bubble-shape regimes.

2 Numerical method

In this section we describe a general computational strategy capable of modelling any kind of two-fluid interfacial flows (see (Smolianski 2001)). The dynamics of a gas bubble in a liquid can, thus, be considered as a particular application of this computational approach.

We start with the specification of the physical assumptions used to derive a suitable mathematical model for our problem. We consider an unsteady laminar flow of two immiscible fluids. Both fluids are assumed to be viscous and Newtonian. Moreover, we suppose that the flow is isothermal, thus neglecting the viscosity and density variations due to changes of a temperature field. We assume also that the fluids are incompressible. The validity of this assumption

is affected by several factors, the most important of which is the condition for Mach number to be smaller than, approximately, 1/3 (see (Batchelor 1967, §3.6) for a thorough discussion on the incompressibility assumption). That condition is satisfied in our case, since we deal with essentially subsonic flows. Presuming, in addition, the fluids to be homogeneous, we may infer that the densities and viscosities are constant within each fluid. We utilize the sharp-interface (zero interfacial thickness) approach; the density and viscosity have, therefore, a jump discontinuity at the interface (see, e.g., (Batchelor 1967)). We assume that the interface has a surface tension. We also suppose that there is no mass transfer through the interface (i.e. the interface is impermeable), and there are no surfactants present in the fluids (hence, there is no species transport along the interface). Under such conditions we do not have to consider the variations of surface tension coefficient in tangential to the interface direction, i.e. the solutocapillary Marangoni effect (the thermocapillary Marangoni effect has been excluded by the assumption on isothermal character of the flow). Therefore, the surface tension coefficient may be assumed constant.

Suppose that the motion of two viscous immiscible fluids under our investigation is confined to some box (a parallelepiped in 3D, a rectangle in 2D). Note that we consider only 2D case here, but the proposed approach is extendible to 3D situation, since the level set approach does not essentially depend on the dimension (see e.g. (Sethian 1999), (Osher & Fedkiw 2002)). The extension to 3D is straightforward in principle, but naturally requires more computational resources.

The boundary of the box can be physical (e.g., the walls of a container), artificial (if we consider a flow in unbounded domain) or partly artificial. In fact, we can always restrict ourselves to some bounded region of interest and consider, then, the flow in that region only. On the other hand, this enables us to avoid dealing with asymptotics at infinity and to make the problem more tractable from computational viewpoint. We denote the boundary of the box by Σ, the domains occupied with the fluids by Ω_1 and Ω_2 and the interface between the fluids by Γ ($\Gamma = \partial\Omega_1 \cap \partial\Omega_2$, where $\partial\Omega_i$ is the boundary of $\Omega_i, i = 1, 2$). Let also Ω be the entire region occupied with the fluids, i.e. the interior of the box ($\Omega = \Omega_1 \cup \Omega_2 \cup \Gamma$). The domains Ω_1 and Ω_2 may be multiply connected, and the interface Γ may intersect the box boundary Σ.

Taking into account the physical assumptions considered above, we may assert that the flow of both fluids is governed by the incompressible Navier-Stokes equations

$$\rho(\mathbf{x}) \left(\frac{\partial \mathbf{v}}{\partial t} + \mathbf{v} \cdot \nabla \mathbf{v} \right) - \tag{1}$$

$$\nabla \cdot (2\mu(\mathbf{x})\underline{\underline{\mathbf{S}}}) + \nabla p = \rho(\mathbf{x})\mathbf{g}\,,$$

$$\nabla \cdot \mathbf{v} = 0 \qquad \text{in } \Omega\,,\ t > 0 \tag{2}$$

supplemented with the interfacial conditions

$$\begin{aligned} &[\mathbf{v}]|_\Gamma = 0\,, \\ &[-p\underline{\underline{\mathbf{I}}} + 2\mu\underline{\underline{\mathbf{S}}}]|_\Gamma \cdot \mathbf{n} = \kappa\sigma\mathbf{n}\,. \end{aligned} \tag{3}$$

Here the density $\rho(\mathbf{x}) = \rho_1$ in Ω_1 and ρ_2 in Ω_2, the viscosity $\mu(\mathbf{x}) = \mu_1$ in Ω_1 and μ_2 in Ω_2, $\mathbf{g}$ is the acceleration of gravitational field, $\underline{\underline{\mathbf{S}}} = \frac{1}{2}(\nabla\mathbf{v} + (\nabla\mathbf{v})^T)$ is the deformation rate tensor, $\underline{\underline{\mathbf{I}}}$ is the identity tensor, σ is the coefficient of surface tension, κ is twice the mean curvature of the interface, $\mathbf{n}$ is the unit normal to the interface, and $[...]|_\Gamma$ denotes a jump across the interface Γ.

It is worth noticing that the first of the interfacial conditions (3) means the continuity of the fluid velocity across the interface, while the second condition shows that the jump of the stress vector at the interface is caused by the surface tension (capillary) force.

The equations (1)–(2) and interfacial conditions (3) should be complemented with the initial conditions

$$\Gamma|_{t=0} = \Gamma^{(0)} \tag{4}$$

$$\mathbf{v}|_{t=0} = \mathbf{v}^{(0)} \quad \text{in } \Omega^{(0)}\,, \tag{5}$$

where $\Gamma^{(0)}$ is the initial position of the interface determining initial shapes of the domains $\Omega_1^{(0)}$ and $\Omega_2^{(0)}$. In addition, the boundary conditions for velocity must be given on Σ. In the case of rising bubble(s), the boundary conditions are given as follows: on the box bottom, the "no-slip" condition is prescribed (both components of velocity are equal to zero); on the walls, the "free-slip" condition is prescribed (normal component of velocity is equal to zero, and tangential component of the stress vector is equal to zero); on the upper boundary of the box, the "outflow" condition is given (i.e. both normal and tangential components of the stress vector are equal to zero).

Obviously, we have three unknowns here: the velocity of fluid $\mathbf{v}(\mathbf{x}, t)$, the pressure $p(\mathbf{x}, t)$ and the interface $\Gamma(\mathbf{x}, t)$. The position of the interface at any moment of time can be determined using the fact that, in the absence of mass transfer through the interface (see the first of the interfacial conditions (3)), the interface is convected by the fluid, i.e. the interface normal velocity is equal

to the normal component of fluid velocity (the latter is continuous across the interface, see (3)).

The problem at hand contains three key ingredients: (i) flow equations (i.e. the Navier-Stokes equations with discontinuous coefficients and singular capillary force), (ii) moving interface and (iii) coupling between velocity-pressure fields and the interface (through the coefficients, capillary force and interfacial advective velocity). To attack the problem numerically we advocate the operator-splitting approach; namely, at each time step, we first resolve the Navier-Stokes system with fixed known interface, then, using computed velocity field, we find the new approximation of the interface. Having found the new interface position we can calculate its normal and curvature, and, thus, evaluate the surface tension force and the density/viscosity coefficients to be used on the next time step in the Navier-Stokes equations.

Discretization of the Navier-Stokes equations

Using the Marchuk-Yanenko fractional-step scheme (see, (Yanenko 1971), (Marchuk 1975)) we may separate the convective nonlinearity, viscous diffusion and incompressibility from one another and treat each of them with corresponding numerical technique. Thus, on each time interval $[t_n; t_{n+1}]$ the Navier-Stokes (NS) system (1)–(3) is approximated by a sequence of three subproblems:

1. NS-convection step

$$\begin{aligned}
&\frac{\partial \mathbf{v}}{\partial t} + \mathbf{v}\cdot\nabla\mathbf{v} = 0 \qquad \text{in} \\
&\Omega \times (t_n; t_{n+1})\,, \\
&\mathbf{v}|_{t=t_n} = \mathbf{v}^n\,, \\
&\Longrightarrow \mathbf{v}^*\,.
\end{aligned} \tag{6}$$

2. Viscous step

$$\begin{aligned}
&\rho(\mathbf{x})\frac{\partial \mathbf{v}}{\partial t} - \nabla\cdot(2\mu(\mathbf{x})\underline{\underline{\mathbf{S}}}) = \rho(\mathbf{x})\mathbf{g} \\
&\quad \text{in } \Omega \times (t_n; t_{n+1})\,, \\
&[\mathbf{v}]|_\Gamma = 0\,, \quad [2\mu\underline{\underline{\mathbf{S}}}]|_\Gamma\cdot\mathbf{n} = \kappa\sigma\mathbf{n}\,, \\
&\quad \text{on } \Gamma\,, \\
&\mathbf{v}|_{t=t_n} = \mathbf{v}^*\,, \\
&\Longrightarrow \mathbf{v}^{**}\,.
\end{aligned} \tag{7}$$

3. Projection step

$$\begin{aligned}
&\frac{\partial \mathbf{v}}{\partial t} + \frac{1}{\rho(\mathbf{x})}\nabla p = 0\,, \\
&\nabla\cdot\mathbf{v} = 0 \qquad \text{in } \Omega \times (t_n; t_{n+1})\,, \\
&[\mathbf{v}]|_\Gamma\cdot\mathbf{n} = 0\,, \quad [p]|_\Gamma = 0 \quad \text{on } \Gamma\,,
\end{aligned} \tag{8}$$

$$\mathbf{v}|_{t=t_n} = \mathbf{v}^{**}\,,$$
$$\Longrightarrow \mathbf{v}^{n+1}\,,\ p^{n+1}\,.$$

Here $\mathbf{v}^n(\mathbf{x})$ and $p^n(\mathbf{x})$ are the approximations to $\mathbf{v}(\mathbf{x}, t_n)$ and to $p(\mathbf{x}, t_n)$, $n = 0, 1, \ldots$, respectively, and $\mathbf{v}^0 \equiv \mathbf{v}^{(0)}$. Each of three subproblems must be complemented by suitable boundary conditions which will be discussed below. The general strategy consists in resolving the steps successively; moreover, each step can be treated with its own time discretization scheme employing a specific (variable) time-step size dictated by stability and/or accuracy reasons. Thus, the given global time step $\Delta t = t_{n+1} - t_n$ may be subdivided into smaller time steps within each of the subproblems.

The operator-splitting implies a decomposition of the interfacial conditions. The splitting of the interfacial stress jump condition indicates that the surface tension balances the jump of viscous stress only (subproblem 2), while the pressure is simply continuous across the interface (subproblem 3). Such approximation of the interfacial condition seems to be in contradiction with the fact that the pressure does have a jump discontinuity at the interface, which can be clearly seen from the famous Laplace-Young equation, if the viscosity is very small. However, we will demonstrate in numerical tests that chosen scheme is capable of capturing the pressure interfacial discontinuity with a good accuracy; thus, there is no need to enforce the discontinuity explicitly (see also the discussion in (Smolianski 2001)).

All the subproblems (7)–(8) are discretized in space by the finite element method using a single uniform triangulation for both velocity and pressure. If we denote the triangulation by $\mathcal{T}_h$, where h is the mesh size (i.e. the maximal diameter of the triangles), the approximation space for the pressure can be defined as

$$Q^h = \{p_h \in C^0(\overline{\Omega}) \Big|\, p_h|_T \in \mathbb{P}_1 \quad \forall T \in \mathcal{T}_h\}\,, \tag{9}$$

where $\mathbb{P}_1$ is the space of polynomials in two variables of degree less than or equal to 1. The discrete velocity belongs to the following space:

$$\mathbf{V}^h = \{\mathbf{v}_h \in \mathbf{C}^0(\overline{\Omega}) \Big| \quad \mathbf{v}_h|_T \in \mathbb{P}_* \times \mathbb{P}_* \,\forall T \in \mathcal{T}_h\}\,, \tag{10}$$

where $\mathbb{P}_*$ is defined as (a) $\mathbb{P}_* \equiv \mathbb{P}_1$ or (b) $\mathbb{P}_* \equiv \mathbb{P}_1^b$ or (c) $\mathbb{P}_* \equiv \mathbb{P}_2$. Here $\mathbb{P}_1^b = \mathbb{P}_1 \bigoplus \mathrm{span}\{\lambda_1\lambda_2\lambda_3\}$ ($\lambda_i\,,\ i = 1, 2, 3$, are the area (barycentric) coordinates on the triangle T), and $\mathbb{P}_2$ is the space of polynomials in two variables of degree less than or equal to 2. In the case (a) we deal with the $\mathbb{P}_1/\mathbb{P}_1$ finite element

for the velocity and pressure, in the case (b) with the so-called "mini" finite element, and in the case (c) with the "Taylor-Hood" finite element (see, e.g., (Quarteroni & Valli 1994)). It is worth noting that the "mini" and "Taylor-Hood" elements satisfy the LBB (*inf-sup*) condition, while the equal-order ($\mathbb{P}_1/\mathbb{P}_1$) approximation does not. However, in combination with the operator-splitting (7)–(8) (which is, in fact, a continuous version of the well-known Chorin projection scheme), the $\mathbb{P}_1/\mathbb{P}_1$ approximation is stable, if the time step $\Delta t \geq Ch^2$ (C is a constant), see, e.g., (Guermond & Quartapelle 1998). This fact enables us to use the most economical but sufficiently accurate $\mathbb{P}_1/\mathbb{P}_1$ approximation for the velocity and pressure.

Now we address briefly the solution of the subproblems (7)–(8). The Navier-Stokes convection step is the first-order nonlinear hyperbolic problem, and, thus, the boundary conditions consist of prescribing the fluid velocity only on the inflow part of the boundary Σ (i.e. where the fluid velocity is directed inward the domain Ω). Then the problem is solved with the explicit Taylor-Galerkin scheme of (Quartapelle & Selmin 1993).

The viscous step requires the boundary conditions to be as for the complete problem. The use of the finite element method for spatial discretization of the viscous step is very essential, since in the weak (variational) formulation, on which the method relies, the interfacial stress jump condition becomes a *natural* condition. Thus, after multiplying (7) with weighting function $\mathbf{w}$ and integrating in Ω by parts, the surface tension force becomes automatically incorporated into the variational formulation:

$$
\begin{aligned}
&\int_{\Omega} \rho(\mathbf{x}) \frac{\partial \mathbf{v}}{\partial t} \cdot \mathbf{w}\, dx + \\
&\int_{\Omega} 2\mu(\mathbf{x}) \underline{\underline{\mathbf{S}}} \cdot\cdot \nabla \mathbf{w}^T\, dx = \\
&\int_{\Omega} \rho(\mathbf{x}) \mathbf{g} \cdot \mathbf{w}\, dx + \\
&\int_{\Gamma} \kappa \sigma \mathbf{n} \cdot \mathbf{w}\, d\Gamma\,.
\end{aligned}
\tag{11}
$$

So we arrive at the "weak" (variational) formulation that is standard for 2nd-order elliptic problems with interfacial conditions (here we treat the velocity time-derivative simply as a zero-order term). Note that the integration by parts is done before any spatial discretization and, thus, independent of the position of the interface with respect to the element boundaries (see the discussion in (Smolianski 2001) for some more details).

The method does not require to approximate a delta-function as it is usually done for accounting of singular capillary force (see, e.g., (Sussman et al. 1994), (Unverdi & Tryggvason 1992)) and, hence, precludes the interface smearing. If the interface Γ can be localized "precisely" (i.e. with the accuracy of the discretization scheme), then a sharp interface may be maintained, and the error in the interface location may be expected to be of the order of the discretization error. Particularly, the second-order accuracy in space can be recovered with the piecewise linear interpolation of all variables (velocity, pressure, interface). Another advantage of the considered approach consists in alleviating the singularity connected with the differentiation of discontinuous viscosity coefficient; in fact, this problem is completely eliminated with the formulation (11).

After an implicit temporal discretization of (11) with the backward Euler or the Crank-Nicolson scheme, we obtain a linear algebraic system having symmetric and positive-definite matrix, which could be successfully solved, for instance, by incomplete Cholesky preconditioned conjugate gradient method.

The projection step defines an inviscid flow problem, thus, the boundary conditions consist in prescribing the boundary values only for the normal component of fluid velocity on Σ. After implicit time-discretization with the time step Δt the problem can be recast in the form of a Poisson-type equation for the pressure endowed with the homogeneous Neumann boundary condition

$$-\nabla \cdot (\frac{1}{\rho(\mathbf{x})} \nabla p^{n+1}) = -\frac{1}{\Delta t} \nabla \cdot \mathbf{v}^{**} \quad \text{in } \Omega\,, \tag{12}$$

$$\mathbf{n} \cdot \nabla p^{n+1}|_{\Sigma} = 0\,, \tag{13}$$

where $\mathbf{v}^{**}$ is the intermediate velocity obtained on the viscous step. The final divergence-free velocity $\mathbf{v}^{n+1}$ is then derived as

$$\mathbf{v}^{n+1} = \mathbf{v}^{**} - \Delta t \frac{1}{\rho(\mathbf{x})} \nabla p^{n+1}\,. \tag{14}$$

Approximation of the interface

We use the level-set approach (see (Osher & Sethian 1988), (Sethian 1999)) for capturing the interface Γ. The approach consists in specifying a continuous "level-set function" Φ such that Φ is the signed distance to the interface Γ, $\Phi > 0$ in Ω_2 and $\Phi < 0$ in Ω_1. Obviously, we have $\Gamma = \{\mathbf{x} |\, \Phi(\mathbf{x}, t) = 0 \; \forall t \geq 0\}$ and $|\nabla \Phi| = 1$ in Ω.

Since the interface is convected with the fluid velocity, the following evolution equation for $\Phi(\mathbf{x}, t)$ can be easily derived (see, e.g., (Chang et al. 1996)):

$$\frac{\partial \Phi}{\partial t} + \mathbf{v} \cdot \nabla \Phi = 0 \quad \text{in } \Omega\,,\ t > 0\,. \tag{15}$$

We solve this pure advection equation with the fluid velocity $\mathbf{v}$ found as the solution of the Navier-Stokes system and with the same explicit Taylor-Galerkin scheme of Quartapelle & Selmin as on the Navier-Stokes convection step. The continuous piecewise-linear approximation is utilized for Φ on the same uniform grid that is used for velocity-pressure approximation. Such approximation allows us to easily localize the interface at any moment of time: indeed, the intersection of the approximate level-set function with each triangle of the grid is just a line segment possibly degenerated to a point (a vertex of the triangle); moreover, to find this line segment one has to determine only the intersection points of the approximate, linear level-set function with triangle's edges. Thus, using piecewise linear continuous approximation for the level-set function on simplicial mesh, we obtain *unique* piecewise linear representation for the interface Γ.

Summary of the algorithm

Our computational approach for numerical modelling of interfacial flows can be summarized as follows:

Step 0. Initialization of the level-set function and velocity.
For each n-th time-step, $n = 1, 2, \ldots$:

1. Computation of interface normal and curvature.
2. Navier-Stokes convection step.
3. Viscous step.
4. Projection step.
5. Level-set convection step.
6. Reinitialization step.
7. Level-set correction step.

The steps 1.–7. are performed successively, and each of the steps 2.–5. may use its own local time-increment size. On each step the *last* computed velocity is exploited; the viscous and projection steps use the interface position found on the previous global time-step. It is also noteworthy that the steps 5.–7. can be computed in a fully parallel manner with the step 2. The whole algorithm is very flexible; it permits, for instance, to compute unsteady interfacial Stokes flow just by omiting the Navier-Stokes convection step.

3 Bubbles in different shape regimes

Fig. 1 shows the typical bubble shapes and velocity streamlines in the frame of reference of the bubble. The comparison with the available experimental data (see, e.g., (Clift et al. 1978)) enables us to conclude that all basic shapes are successfully recovered with the physical parameters having realistic values. Our results are also in a good agreement with the experimental predictions of (Bhaga & Weber 1981). In (Smolianski et al. 2003) the detailed analysis on the differencies and similiarities of bubble shape regimes is provided.

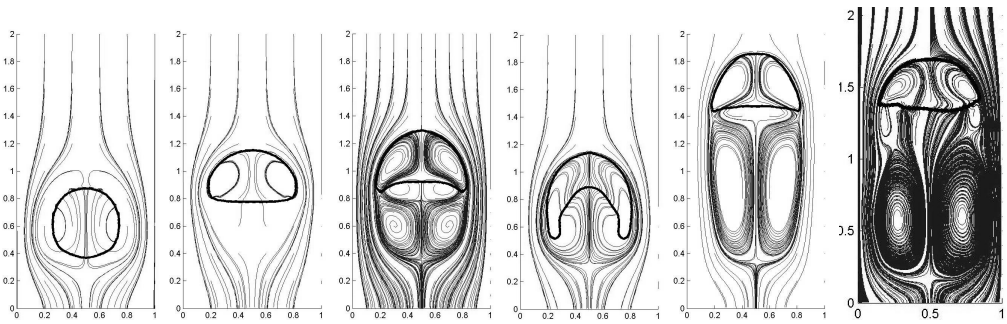

(a) (b) (c) (d) (e) (f)

Fig. 1. Different computed shapes of bubbles: (a) spherical with Re=1, Eo=0.6, (b) ellipsoidal with Re=20 Eo=1.2, (c) dimpled ellipsoidal cap with Re=35, Eo=125, (d) skirted with Re=55, Eo=875, (e) spherical cap with Re=94, Eo=115 and (f) wobbling with Re=1100, Eo=3.0; $\rho_1/\rho_2 = 10^3$; $\mu_1/\mu_2 = 10^2$.

4 Vortex shedding

Vortex shedding phenomena can be observed in different bubble flow regimes, but the case of a wobbling bubble exhibits the most pronounced unsymmetric vorticity pattern in the bubble wake and, at the same time, is the most difficult for numerical simulations owing to its notorious interface-instability. The wobbling typically appears with sufficiently high Reynolds numbers when the Eötvös number is, roughly, in the range between 1 and 100 (see (Clift et al. 1978)).

Since the typical range for the Reynolds number corresponding to the wobbling motion is approximately the same as for the spherical cap regime, the wobbling bubble (see Fig. 2) retains a nearly spherical cap shape. However, at later stage of the motion, a remarkable flattening of the bubble top can be observed (Fig. 2). The bubble bottom undergoes permanent deformations resulting from the unstable and unsymmetric evolution of the bubble wake. In particular, the

unsymmetric pairs of secondary vortices are clearly observed in the wake as the consequence of asynchronous separation of the boundary layer from different sides of the bubble surface. This flow pattern bears some resemblance to the von Karman vortex path typically formed behind a rigid body in a highly convective flow.

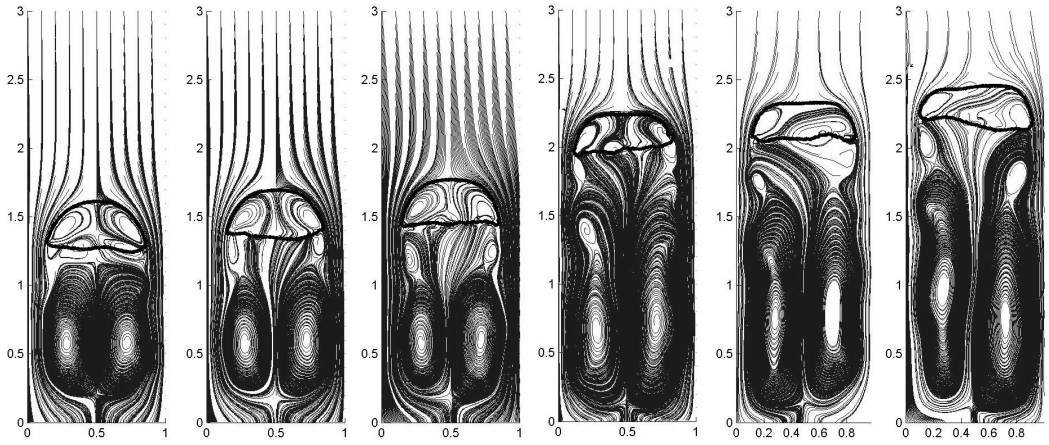

Fig. 2. The rise of a wobbling bubble. Re=1100, Eo=3.0, $\rho_1/\rho_2 = 10^3$, $\mu_1/\mu_2 = 10^2$.

With lower Reynolds and higher Eötvös numbers, one can observe even more pronounced wake instability (see Fig. 3; in this simulation the liquid has the same properties as water but the gas is ten times more dense than air). While the wobbling of the bubble bottom remains apparent, the flattening of the bubble top is not seen, which makes the bubble shape resemble a spherical cap. The remarkable bubble wake, known in the literature as helical vortex path, is in a good qualitative agreement with experimental investigations of (Tsuchiya & Fan 1988).

An experiment with a high Reynolds number, namely $Re = 5500$, is shown in Figures 4–6. The surface tension is much smaller here than in the wobbling regime (Eo is higher), and the bubble exhibits a rather irregular variant of the spherical-cap shape. However, the bubble does not remain within the spherical-cap regime but tend to vary from the spherical-cap to the skirted shape. Once the bubble becomes skirted, the skirt quickly breaks off due to the action of the wake vortices and the bubble regains the spherical-cap shape. The first break-up of a bubble can be seen in Figure 4b, the second in 4i, the third in Figure 5i and the fourth in Figure 6e. During the break-up, a "bubble ring" is detached from the bubble (our two-dimensional figures show the "cross-section" of the ring in the form of two small bubbles); the detached bubble ring remains in the wake of the main bubble and does not affect the bubble's dynamics. Unfortunately, due to the limitations on the grid density we are not able to simulate the small bubble rings in long-run computations. The qualitative picture of the bubble break-up is in a full agreement with experimental observations of (Hnat & Buchmaster 1976). Our results also

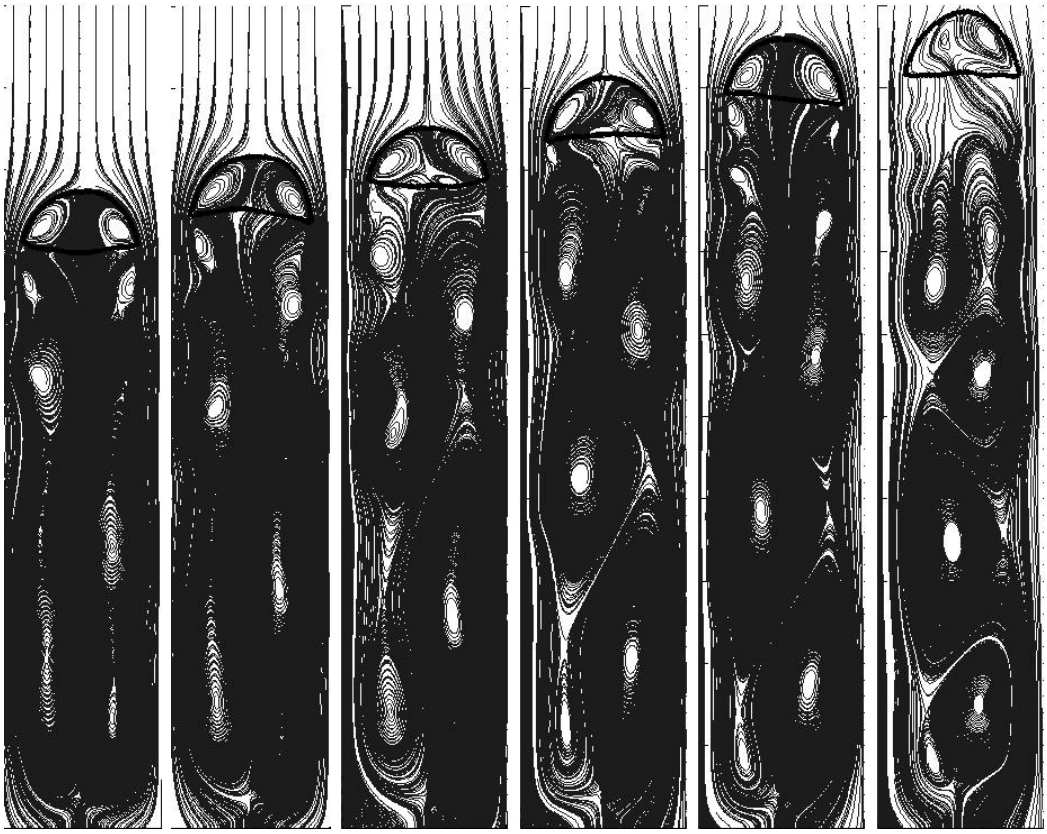

Fig. 3. Helical vortex path behind the bubble. $Re = 900$, $Eo = 20.2$, $\mu_1/\mu_2 = 10$, $\rho_1/\rho_2 = 10^2$.

compare well with the 2D numerical results of (Sussman et al. 1994), who employed the finite difference level-set method, and with the 2D numerical predictions of (Baker & Moore 1989), who advocated the boundary integral method for an inviscid gas bubble.

One can also observe the vortex pairs discharging from the bubble edge in Figures 4–6. The first discharge can be seen approximately in Figure 5a and the second almost straight after the first in Figure 5c. The vortices shed from the bubble edge tend to merge forming a single big vortex pair. The third discharge of vorticity takes a little longer (it can be seen in Figure 6a), while the fourth happens rather quickly after the third (Figure 6f). The process of merger of the newly formed vortex pairs with the main wake vortices results in a significant dilation of the wake, which, finally, implies a wake fragmentation (see Figure 6h).

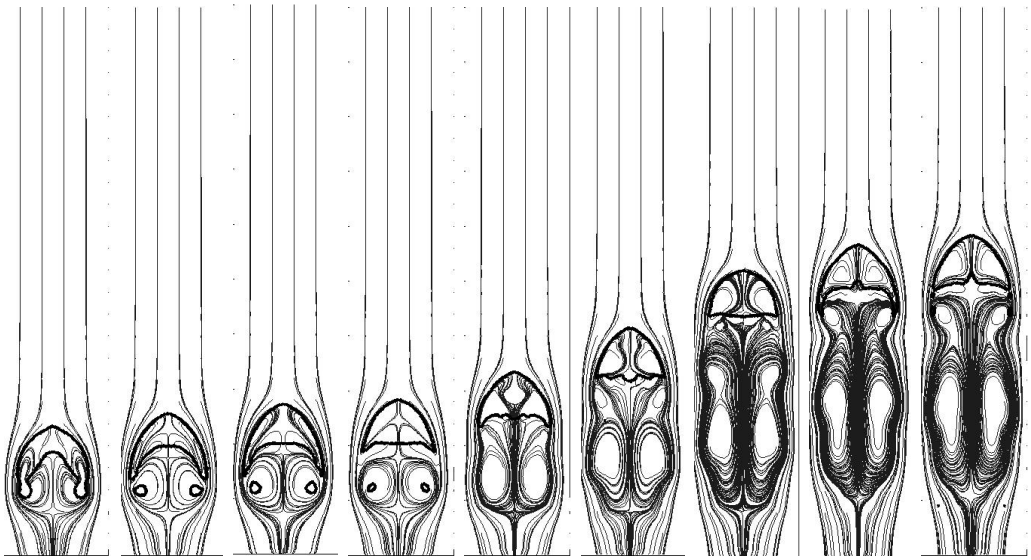

(a) (b) (c) (d) (e) (f) (g) (h) (i)

Fig. 4. The rise of a bubble at high Reynolds number (1). $Re = 5500$, $Eo = 600$, $\mu_1/\mu_2 = 10$, $\rho_1/\rho_2 = 10^2$.

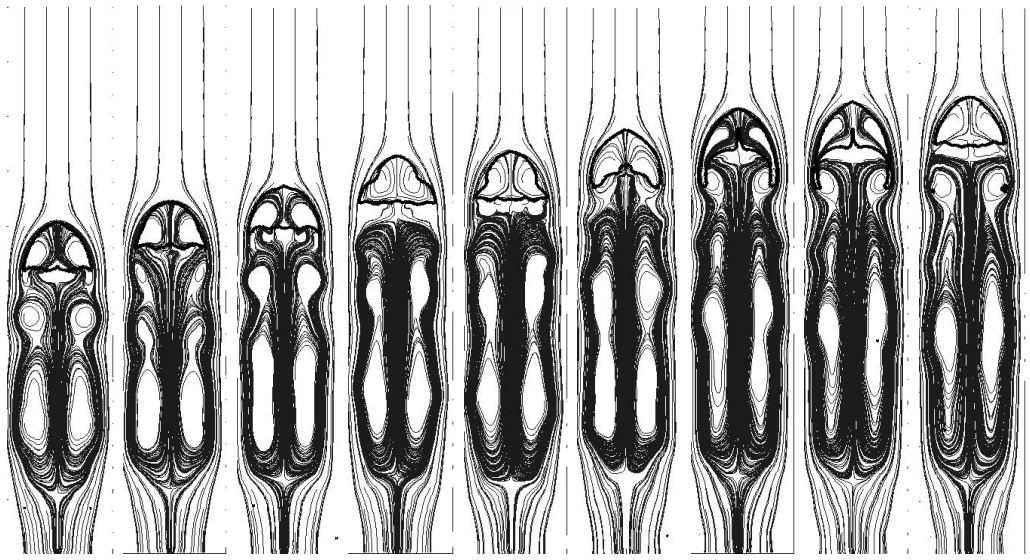

(a) (b) (c) (d) (e) (f) (g) (h) (i)

Fig. 5. The rise of a bubble at high Reynolds number (2). $Re = 5500$, $Eo = 600$, $\mu_1/\mu_2 = 10$, $\rho_1/\rho_2 = 10^2$.

5 Results on coalescence of bubbles

We consider the rectangular domain of the unit width with two initially circular bubbles inside; the radius of both bubbles is equal to 0.25. Bubbles have

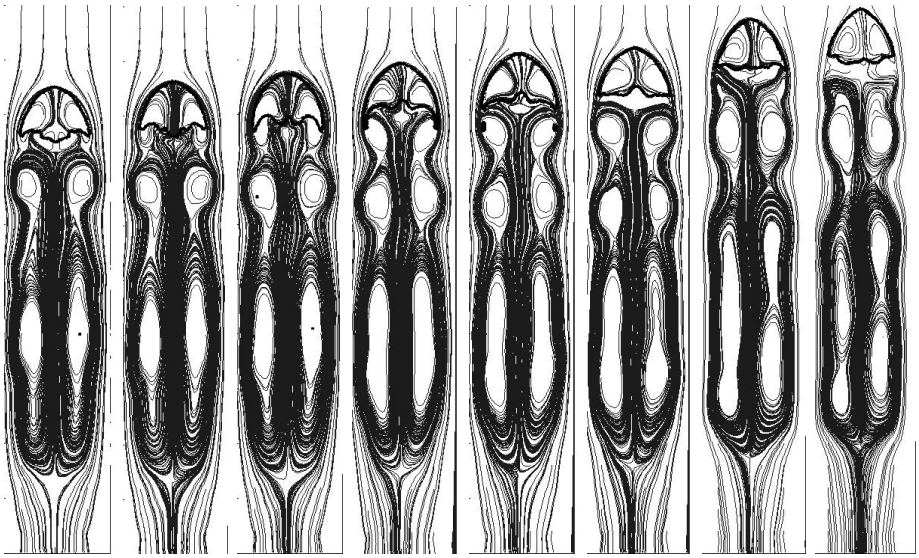

(a) (b) (c) (d) (e) (f) (g) (h)

Fig. 6. The rise of a bubble at high Reynolds number (3). $Re = 5500$, $Eo = 600$, $\mu_1/\mu_2 = 10$, $\rho_1/\rho_2 = 10^2$.

a common axis of symmetry. We prescribe zero velocity field at the initial moment. The dynamics of the bubbles, to a large extent, depends on the initial distance between them and on the magnitude of the surface tension. If the surface tension is high enough, no merger happens, the bubbles develop nearly ellipsoidal shapes and rise separately (see, e.g., (Unverdi & Tryggvason 1992)). Hence, in order to simulate a merger process, we take comparably small surface tension coefficient.

Figures 7–12 illustrate the process of bubble merger in different shape regimes.

During the rise of the bubble, two opposite signed vortices are created in the wake of the larger bubble. This produces a lower pressure region behind the large bubble and generates flow streaming into the symmetry line of the flow. As a result, the front portion of the small bubble becomes narrower and sharper. The head of the lower bubble almost catches up with the bottom of the upper one. In the next moment, the two bubbles merge into a single bubble. At this time, the interface conjunction forms a cusp singularity that is rapidly smoothed out by viscosity and surface tension.

Bubble coalescence in spherical shape regime is shown in Fig. 7. Due to considerable rigidity of the bottom of the upper bubble, the liquid rather quickly becomes squeezed out of the space between the bubbles, and the bubbles merge.

In ellipsoidal shape regime (see Fig. 8), the bottom of the upper bubble de-

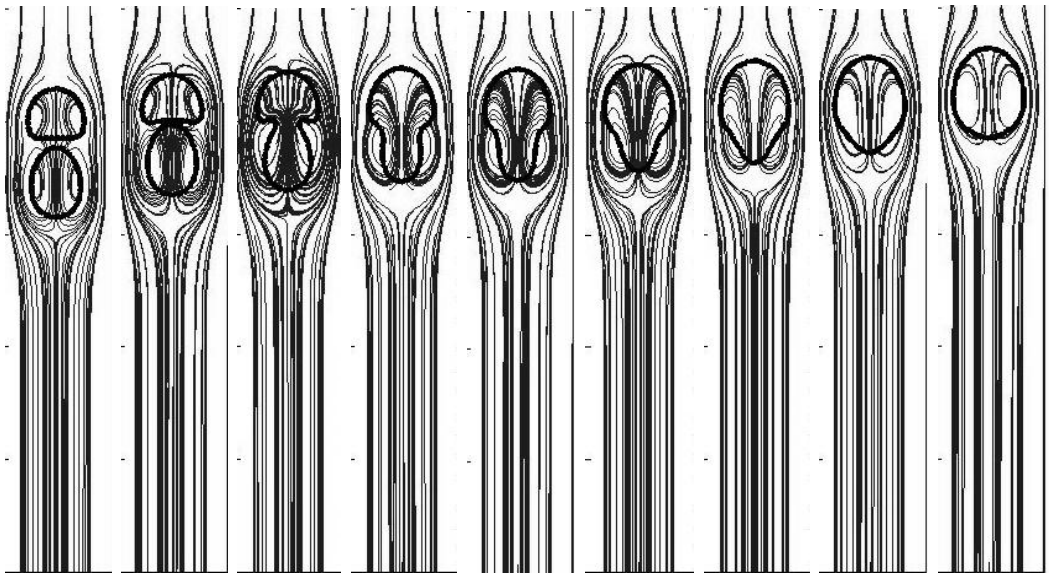

(a) (b) (c) (d) (e) (f) (g) (h) (i)

Fig. 7. Merger of two spherical bubbles. $Re = 2$, $Eo = 1.2$, $\rho_1/\rho_2 = 10^2$, $\mu_1/\mu_2 = 10$.

forms under the influence of the lower bubble, thus, making it possible to preserve a thin liquid film between the bubbles. The upper bubble develops a dimpled-ellipsoidal rather than an ellipsoidal shape. When the bottom of the upper bubble cannot deform any more, the liquid film between the bubbles starts getting thinner, and, finally, the lower bubble merges with the upper one.

Bubble coalescence in the dimpled ellipsoidal shape regime (Fig. 9) apparently differs from the previous two regimes because of the strong influence of the upper bubble's wake. The wake behind a dimpled-ellipsoidal bubble is longer than the wake behind an ellipsoidal one, and the weak secondary vortices appear right under the bubble bottom (see Fig. 1c). When the lower bubble catches up with the upper bubble's wake it starts to rise much faster and its top becomes narrower. The lower bubble tends to merge with the upper one, but the secondary recirculation under the bottom of the upper bubble precludes an immediate merger. The front of the lower bubble stretches along the bottom of the upper bubble, and, in the next moment, the lower bubble's top merges with the center of the upper bubble's bottom. The recirculating liquid between the bubbles is rapidly squeezed out, and the bubbles form a single, dimpled ellipsoidal bubble. The simulations of merging dimpled-ellipsoidal bubbles like the one in Fig. 9 are very important for understanding the mechanism of the liquid "film thinning" phenomenon.

The considered above bubble coalescence results agree with the computations of (Chang et al. 1996), (Tornberg 2000), (Unverdi & Tryggvason 1992) and

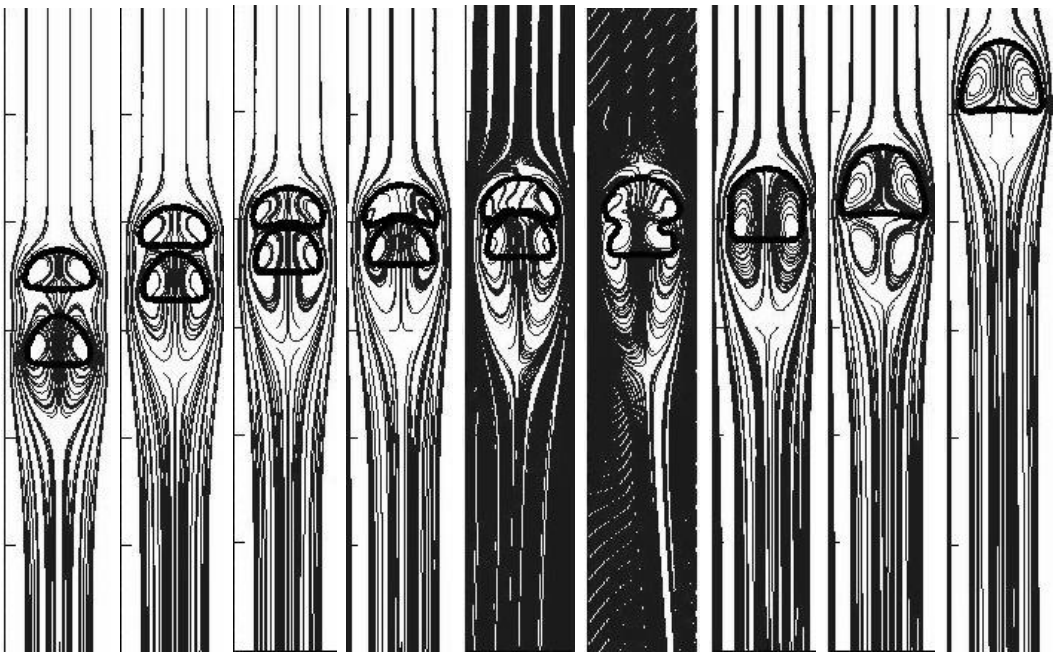

(a) (b) (c) (d) (e) (f) (g) (h) (i)

Fig. 8. Merger of two ellipsoidal bubbles. $Re = 20$, $Eo = 1.2$, $\rho_1/\rho_2 = 10^2$, $\mu_1/\mu_2 = 10$.

compare favourably with the numerical predictions of (Delnoij el al. 1998) who found a qualitative agreement with available experimental data.

Figures 10 – 12 illustrate the coalescence of two wobbling bubbles. At the initial stage of motion, both bubbles undergo almost synchronous shape deformations typical for the wobbling-shape regime. However, as soon as the wake of the upper bubble propagates down toward the lower bubble, the latter accelerates and takes a narrower shape. Being in the wake of the upper bubble the lower one experiences serious deformations and becomes skirted (see Fig. 11). The pronounced elongation of the lower bubble's skirt may be possibly explained by the strong vorticity in the wake of the upper bubble. When the lower bubble comes close enough to the upper one, it regains its characteristic wobbling shape; the bottom of the upper bubble flattens, while the top of the lower becomes sharper. The process of merger seems to be very similiar to the coalescence of two ellipsoidal bubbles (see Fig. 8), but the lower bubble's bottom undergoes significant perturbations (Fig. 12). The newly formed single bubble immediately starts a wobbling-like motion.

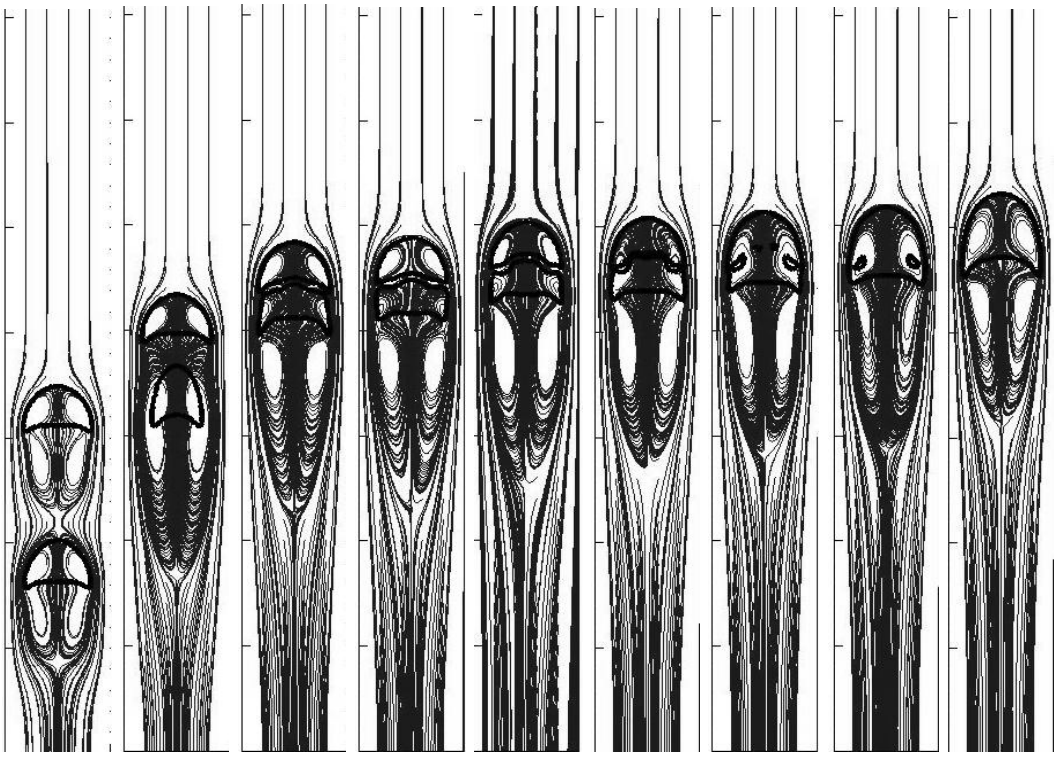

(a) (b) (c) (d) (e) (f) (g) (h) (i)

Fig. 9. Merger of two dimpled ellipsoidal bubbles. $Re = 35$, $Eo = 125$, $\rho_1/\rho_2 = 10^2$, $\mu_1/\mu_2 = 10$.

6 Conclusions

We have presented the results of a computational study on two-dimensional bubble dynamics. Despite the seeming insufficiency of a two-dimensional model for the quantitative analysis of three-dimensional bubble evolution phenomena, we have been able to obtain a good qualitative agreement with the available experimental data. With the presented numerical approach it turned out to be possible to recover all basic shape regimes within the experimentally predicted ranges of problem parameters. In particular, we successfully simulated the wobbling bubble regime remarkable by its unsymmetric vortex pattern and a highly convective nature. To our knowledge, the vortex shedding simulations for a rising wobbling bubble are presented for the first time. It is worth noting that the results of our two-dimensional simulations qualitatively agree very well with the three-dimensional experimental observations of helical vortex paths. The ability to recover the non-symmetric vortex path behind the wobbling bubble seems to be a strength of our algorithm (the axisymmetrical modelling would not allow to achieve this).

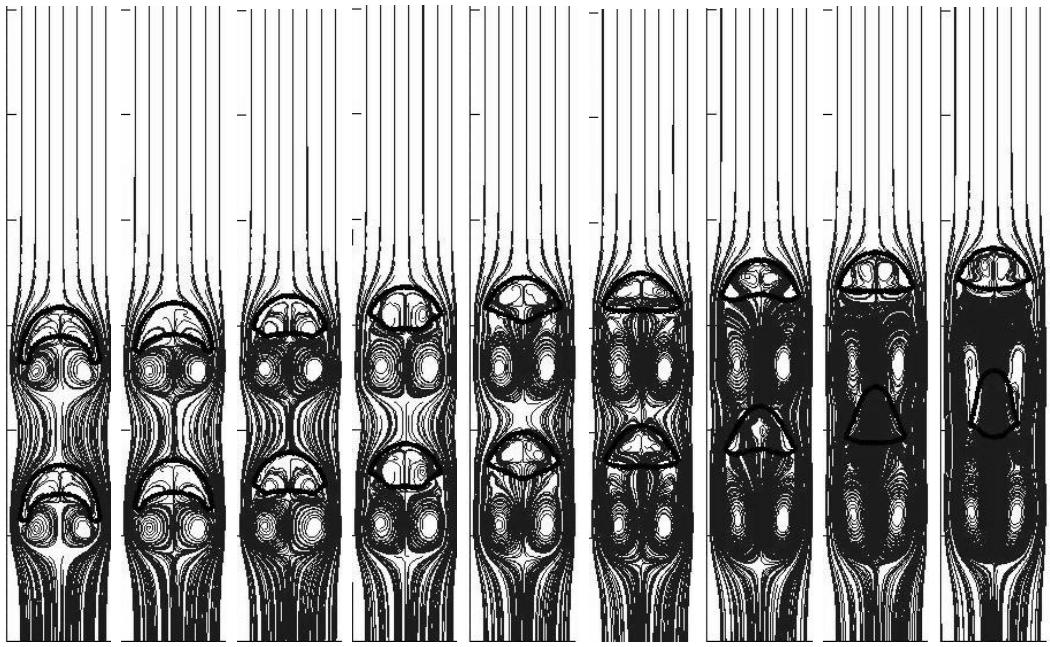

Fig. 10. Merger of two wobbling bubbles (1). $Re = 1813$, $Eo = 8.4$, $\mu_1/\mu_2 = 100$, $\rho_1/\rho_2 = 10$.

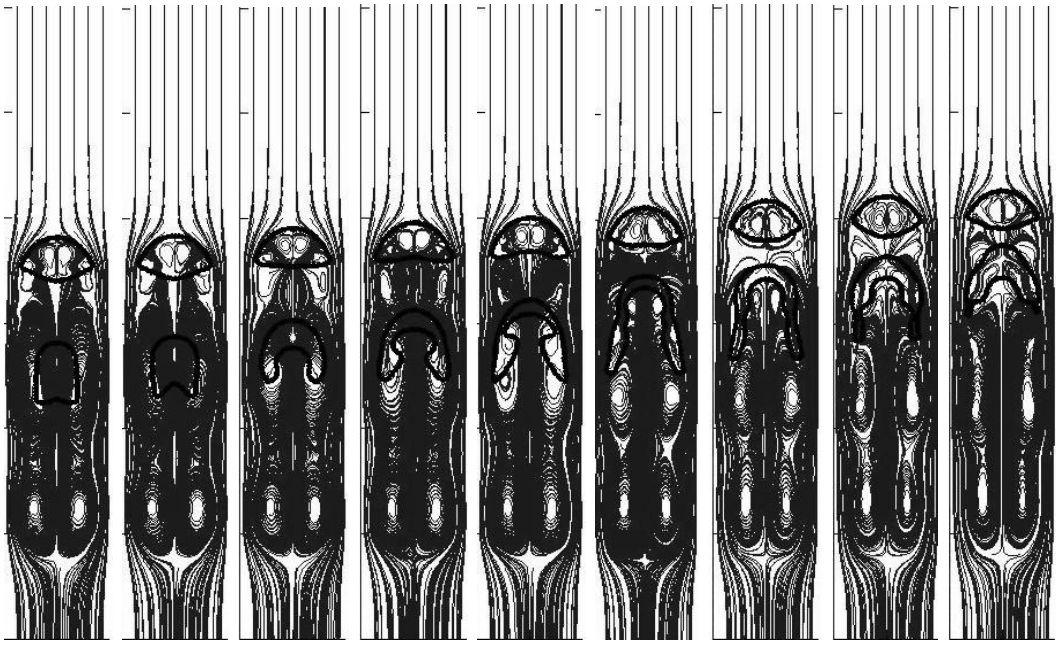

Fig. 11. Merger of two wobbling bubbles (2). $Re = 1813$, $Eo = 8.4$, $\mu_1/\mu_2 = 100$, $\rho_1/\rho_2 = 10$.

The study on the coalescence of bubbles in diverse shape regimes highlights the main differences and similarities of the merger processes. While the results on the merger of two spherical and ellipsoidal bubbles are treated in the literature

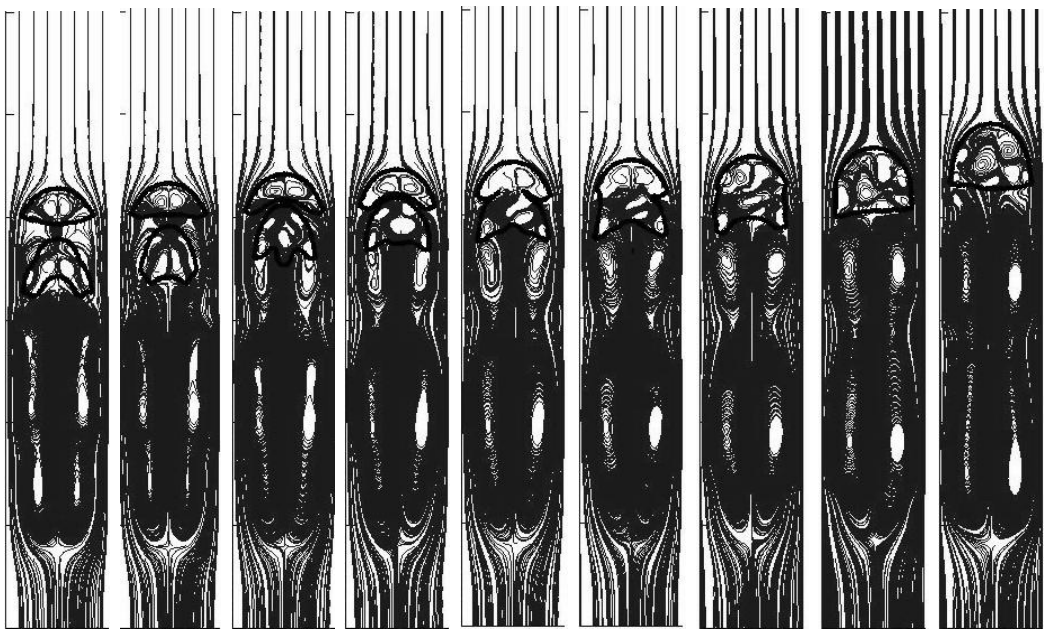

Fig. 12. Merger of two wobbling bubbles (3). $Re = 1813$, $Eo = 8.4$, $\mu_1/\mu_2 = 100$, $\rho_1/\rho_2 = 10$.

(Krishna et al. 1999), we are unaware any works addressing the coalescence of two wobbling bubbles. The proposed computational method clearly demonstrates the ability to cope with the wake and interface instability inherent to the wobbling regime and provides a useful possibility to gain a deeper insight into the physics of the complex bubble-coalescence phenomena. The work on this subject is under way and the results will be reported soon ((Smolianski et al.)).

Acknowledgments

This work was supported by the grant 70139/98 of Tekes, the National Technology Agency of Finland.

References

Baker, G.R. and D.W. Moore, (1989), The rise and distortion of a two-dimensional gas bubble in an inviscid liquid. Phys. Fluids A 1, 1451-1459.

Batchelor, G.K., (1967), An Introduction to Fluid Dynamics. Cambridge University Press.

Bhaga, D. and M.E. Weber, (1981), Bubbles in viscous liquids: shapes, wakes and velocities. J. Fluid Mech. 105, 61-85.

Chang, Y.C., T.Y. Hou, B. Merriman and S. Osher, (1996), A level set formulation of Eulerian interface capturing methods for incompressible fluid flows. J. Comput. Phys. 124, 449-464.

Clift, R.C., J.R. Grace and M.E. Weber, (1978), Bubbles, Drops and Particles. Academic Press.

Delnoij, E., J.A.M. Kuipers and W.P.M. van Swaaij, (1998), Computational fluid dynamics (CFD) applied to dispersed gas-liquid two-phase flows. In: Fourth European Computational Fluid Dynamics Conference ECCOMAS CFD'98, John Wiley & Sons, Chichester, 314-318.

Guermond, J.-L. & L. Quartapelle, (1998) On stability and convergenceof projection methods based on pressure Poisson equation. Int. J. Num. Meth. Fluids 26, 1039–1053.

Hartunian, R.A. and W. R. Sears, (1957), On the instability of small gas bubbles moving uniformly in various liquids. J. Fluid Mech. 3, 27-47.

Hnat, J.G. and J.D. Buckmaster, (1976), Spherical cap bubbles and skirt formation. Phys. Fluid 19, 182-194.

Krishna, R. M.I. Urseanu, J.M. van Baten, J. Ellenberger, (1999), Rise velocity of a swarm of large gas bubbles in liquids. Chemical Engineering Science 54, 171-183.

Marchuk, G.I., (1975), Methods of Numerical Mathematics. Springer.

Moore, D.W., (1959), The rise of a gas bubble in a viscous liquid. J. Fluid Mech. 6, 113-130.

Osher, S. & J.A. Sethian, (1988), Fronts propagating with curvature dependent speed: algorithms based on Hamilton-Jacobi formulations. J. Comput. Phys. 79, 12-49.

Osher, S. & R.P. Fedkiw, (2002), Level Set Methods and Dynamic Implicit Surfaces. Springer-Verlag.

Quartapelle, L. & V. Selmin, (1993) High-order Taylor-Galerkin methods for nonlinear multidimensional problems. In: Finite Elements in Fluids, Pineridge Press, pp. 1374-1384.

Quarteroni, A. & A. Valli, (1994) Numerical Approximation of Partial Differential Equations. Springer-Verlag, Berlin.

Sethian, A.J., (1999), Level Set Methods and Fast Marching Methods: Evolving Interfaces in Computational Geometry, Fluid Mechanics, Computer Vision, and Materials Science. Cambridge University Press.

Smolianski, A., (2001), Numerical Modeling of Two-Fluid Interfacial Flows, PhD thesis, University of Jyväskylä, ISBN 951-39-0929-8.

Smolianski, A., (2003), Numerical simulation of interfacial flows. In: Fourth European Conference on Numerical Mathematics and Advanced Applications ENUMATH 2001 (Eds. F. Brezzi, A. Buffa, S. Corsaro, A. Murli), Springer-Verlag Italia, Milano, 173-179.

Smolianski, A., H. Haario, P. Luukka, (2003), Computational study of bubble dynamics. Submitted to the Journal Computers & Fluids.

Smolianski, A., H. Haario, P. Luukka, Numerical investigation of coalescence of gas bubbles in diverse shape regimes. In preparation.

Sussman, M., P. Smereka and S. Osher, (1994), A level set approach for computing solutions to incompressible two-phase flow. J. Comput. Phys. 114, 146-159.

Taylor, T.D. and A. Acrivos, (1964), On the deformation and drag of a falling viscous drop at low Reynolds number. J. Fluid Mech. 18, 466-476.

Tornberg, A.K., (2000), Interface Tracking Methods with Application to Multiphase Flows. PhD thesis, Royal Institute of Technology, Stockholm.

Tsuchiya, K. & L.-S. Fan, (1988), Near-wake structure of a single gas bubble in a two-dimensional liquid-solid fluidized bed: vortex shedding and wake size variation. Presented at AIChE A. Mtg, Miami Beach, Fla, Paper 10b. Chem. Engng Sci. 43, 1167-1181.

Unverdi, S.O. and G. Tryggvason, (1992), A front-tracking method for viscous, incompressible, multi-fluid flows. J. Comput. Phys. 100, 25-37.

Walters, J.K. and J.F. Davidson, (1962), The initial motion of a gas bubble formed in an inviscid liquid. Part 1. The two-dimensional bubble. J. Fluid Mech. 12, 408-417.

Walters, J.K. and J.F. Davidson, (1963), The initial motion of a gas bubble formed in an inviscid liquid. Part 2. The three-dimensional bubble and the toroidal bubble. J. Fluid Mech. 17, 321-336.

Wegener, P.P. and J.Y. Parlange, (1973), Spherical-cap bubbles. Ann. Rev. Fluid Mech. 5, 79-100.

Yanenko N.N., (1971), The Method of Fractional Steps. Springer-Verlag, Berlin.